A Materials Selection Protocol for Lightweight Actively Cooled Panels

Lorenzo Valdevit
Mechanical and Aerospace Engineering Department,
University of California,
Irvine, CA 92697-3975

Natasha Vermaak

Frank W. Zok

Anthony G. Evans

Materials Department,
University of California,
Santa Barbara, CA 93106-5050

This article provides a materials selection methodology applicable to lightweight actively cooled panels, particularly suitable for the most demanding aerospace applications. The key ingredient is the development of a code that can be used to establish the capabilities and deficiencies of existing panel designs and direct the development of advanced materials. The code is illustrated for a fuel-cooled combustor liner of a hypersonic vehicle, optimized for minimum weight subject to four primary design constraints (on stress, temperatures, and pressure drop). Failure maps are presented for a number of candidate high-temperature metallic alloys and ceramic composites, allowing direct comparison of their thermostructural performance. Results for a Mach 7 vehicle under steady-state flight conditions and stoichiometric fuel combustion reveal that, while C–SiC satisfies the design requirements at minimum weight, the Nb alloy Cb752 and the Ni alloy Inconel X-750 are also viable candidates, albeit at about twice the weight. Under the most severe heat loads (arising from heat spikes in the combustor), only Cb752 remains viable. This result, combined with robustness benefits and fabrication facility, emphasizes the potential of this alloy for scramjets. [DOI: 10.1115/1.2966270]

Keywords: active cooling, lightweight structures, sandwich panels, hypersonics, multifunctional optimization, thermal stresses, materials selection

1 Introduction

Components that experience extreme heat flux, while simultaneously supporting pressure loads, are frequently encountered in aerospace and power systems. In some cases, the challenge can be addressed by using an efficient means for spreading the heat and then convecting or radiating to the environment from a large area. Heat pipes are especially effective for this purpose [1]. This strategy is not always viable, whereupon active cooling by a fluid pumped through the structure is required. In such cases, before embarking on materials development and fabrication, it would be most beneficial to have a procedure that simultaneously selects the preferred material and design, while also highlighting the inadequacies of existing materials. The task is complicated by the intertwining of material properties and geometric parameters. Namely, the optimal geometries depend on materials properties in a highly coupled way. The purpose of this article is to describe the principles governing the development of a code that couples material choices with design parameters and to present an illustration.

The procedure is illustrated for a fuel-cooled combustor liner of a hydrocarbon-powered hypersonic vehicle (Fig. 1) [2,3]. This choice is timely because, while the potential to achieve positive thrust from a scramjet has been recently demonstrated [2–4], selecting materials and generating designs that resist the thermomechanical loads for the duration of a typical mission have proved to be daunting. Some aspects of the design and performance of actively cooled combustion systems have been explored [5–8], including geometry optimization [9–12]. However, a comprehensive treatment that accounts for the complete set of thermomechanical constraints is lacking.

The structure of this article is as follows. A synopsis of the analysis and optimization protocol is outlined in Sec. 2. Analytical models for temperature distributions and thermomechanical stresses are presented in Secs. 3 and 4. Also included are the results from computational fluid dynamics (CFD) and finite element (FE) calculations, designed to critically assess the accuracy of the model predictions and the key underlying assumptions. Formulation of the optimization scheme and its application to a combustor liner of a notional Mach 7 scramjet vehicle are contained in Sec. 5: inclusive of an assessment of the suitability of a wide range of candidate structural materials. The implications for materials selection follow. For facility of presentation, the analytic details are presented in Appendixes.

2 Principles and Procedures

A prototypical combustor wall for an aerospace system (Fig. 1) comprises a sandwich plate subject to three loading mechanisms: external pressure from the combustion gases, internal pressure from the coolant, and thermal loads due to the temperature differences between the combustion side and the vehicle exterior. In addition to the obvious thermostructural requirements (no melting and no yielding/fracture), the design may be limited by fuel-specific constraints (e.g., avoiding coking while promoting cracking) and the need to limit pressure losses in the cooling system.

A variety of shapes can be envisioned for the cooling ducts. Rectangular, triangular, or rhombic cross section can be manufactured to ensure thin walls and are easiest to model analytically. The present study focuses on rectangular ducts. Extension to other periodic shapes is elementary and is not expected to modify the main conclusions.

The protocol employed for thermostructural analysis and design optimization consists of the following steps (Fig. 2). (i) A range is defined for the expected heating loads (represented by the heat transfer coefficient h_G of the hot gases) and the cooling efficiency (represented by the coolant flow rate per unit width of panel, $\dot{V}^{\text{eff}}$). (ii) A candidate material is selected and its physical and mechanical properties either measured or obtained from handbooks. (iii) At each point in $(h_G, \dot{V}^{\text{eff}})$ space, the design parameters are systematically varied over a prescribed range and the temperatures

Contributed by the Applied Mechanics Division of ASME for publication in the Journal of Applied Mechanics. Manuscript received February 24, 2008; final manuscript received June 6, 2008; published online August 22, 2008. Review conducted by Martin Ostoja-Starzewski.

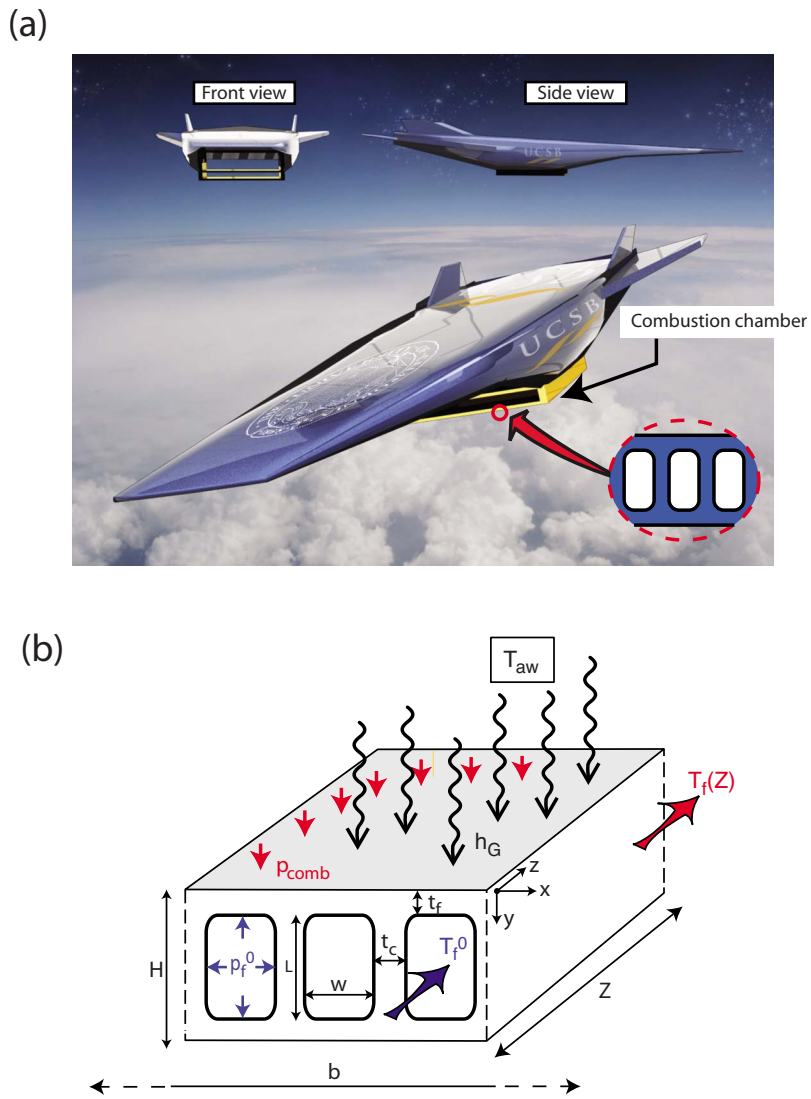

Fig. 1 (*a*) **Artist rendition of a prototypical hypersonic air-breathing vehicle.** (*b*) **Schematic of actively cooled panel with thermostructural loads.**

and stresses calculated for each combination. Upon comparison with material and coolant properties, the viability of the design is ascertained. (iv) provided that solutions exist, the design is optimized for minimum mass, subject to a number of design constraints. Otherwise, if a solution is not found, the point $(h_G, \dot{V}^{\text{eff}})$ is deemed external to the design space. (v) Once the entire design space has been scanned for each candidate material, comparisons are made of materials on the basis of structural robustness (namely, the extent of feasible solution area in $(h_G, \dot{V}^{\text{eff}})$ space) and weight efficiency.

Temperatures in the panel have been derived using a two-dimensional resistance network model and the solutions verified by the CFD and FE calculations. The utility of the temperature predictions is twofold. First, they are used to ensure that the conditions remain within allowable limits for the material and the coolant. Second, they become input for calculation of thermal stresses. To permit formulation of the structural constraints, these stresses are superimposed on those induced by the pressure loads, both external to the liner (inside the combustion chamber) and within the cooling channels. The thermomechanical stresses are required to remain below the local temperature-dependent material strength. A constraint on pressure drop is also imposed.

The assessment facilitates three goals. (i) It determines the relative merits of representative categories of high-temperature materials (Tables 1 and 2), inclusive of refractory alloys and ceramic matrix composites (CMCs). (ii) It provides a focus for the development of advanced materials that outperform existing options. (iii) It assesses the possible benefits of superposing a thermal barrier coating (TBC), such as yttria-stabilized zirconia (YSZ), motivated by the extensive use of such coatings in aeroturbines [13].

3 Temperature Distribution

To obtain analytic estimates of the temperatures, three simplifications are invoked. (i) The top face of the panel is exposed to hot gases at a uniform adiabatic wall temperature T_{aw} and constant heat transfer coefficient h_G, whereas the bottom face and the sides are thermally insulated. Consequently, all of the heat passed through the top face is carried away by the cooling fluid. (ii) No heat is conducted along the length of the panel in either the structure or the coolant. This assumption results in slightly conservative temperature estimates. (iii) The coolant temperature is uniform at each cross section, increasing monotonically with distance z along the panel length from an initial value T_f^o at the channel inlet to its maximum $T_f^{\max}$ at the outlet.

The thermal resistance network is illustrated in Fig. 3 and the solutions for the key temperatures are detailed in Appendix A. The

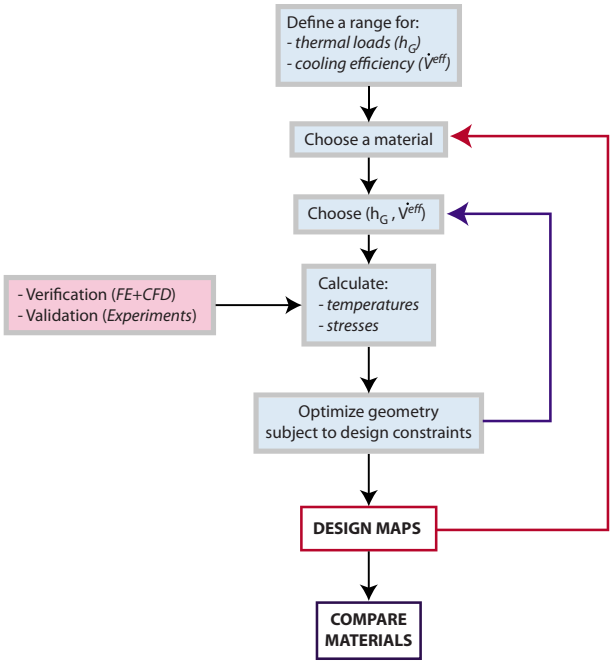

Fig. 2 Schematic of the materials selection procedure

main goals are to ascertain the maximum temperatures in the material $T_m^{\max}$ and in the fuel $T_f^{\max}$. Additionally, for the ensuing determination of thermal stresses, four temperature differences are defined. The first two are those across the top face (in the y-direction): one directly above the core web, ΔT_{tf}^c, and the second at the midpoint between a pair of webs, ΔT_{tf}^w. The second two, $\Delta T_{\text{panel}}^c$ and $\Delta T_{\text{panel}}^w$, are those across the entire panel (also in the y-direction), measured from the middle of the top face to the bottom face, directly above and between the core webs. The analysis indicates that all the preceding temperature differences are greatest at the inlet ($z=0$).

CFD calculations, performed using the commercial code, FLUENT©, were used to assess the uniformity of the heat transfer coefficient around the internal surface of the channel and the effect of longitudinal conduction. The panel used for these calculations has a near-optimal geometry (detailed in Sec. 5) and made from Inconel X-750 (a Ni-based superalloy). Approximate chemical compositions and pertinent material properties are summarized in Tables 1 and 2. The coolant is taken to be JP-7 jet fuel (Table 3). Both the fuel and the solid are meshed using three-dimensional elements. The fuel flow rate and hot gas temperature are selected to be representative of a notional Mach 7 cruise vehicle (Sec. 5). The results (Fig. 4(a)) affirm that h_C is essentially uniform over the interior surface of the top face, where the vast majority of the heat is transferred to the fuel. The variations around the corners and along the core and bottom face are deemed unimportant, because the heat transfer averaged over the channel perimeter conforms to the value obtained from established correlations [14], with an accuracy of about 10%. Additionally, the axial distribution of the section-averaged h_C confirms that full thermal and kinematical developments are attained after the fuel has traveled a distance of a few hydraulic diameters (Fig. 4(b)). Effects of longitudinal conduction within the solid were ascertained by comparing CFD calculations with and without axial conduction. For the parameter values selected, the two sets of results are indistinguishable.

A further assessment of the predicted temperatures was made through FE calculations of the same panel, performed using the ABAQUS© code. The mesh consists of quadratic generalized plane strain elements with reduced integration (CPEG8RHT). Convective boundary conditions are applied both to the top face (h_G =445 W/m^2 K, T_{aw}=3050 K) and the internal channel surfaces (h_C=2266 W/m^2 K, T_f=653 K). The fuel temperature corresponds to the predicted exit temperature for the relevant geometry and boundary conditions, assuming an entry fuel temperature T_f^o =400 K. The remainder of the cell perimeter is thermally insulated.

The steady-state temperature distribution at the channel outlet and the corresponding analytic predictions at eight critical locations are shown in Fig. 5. The comparisons reveal that the maximum temperature in the structure is captured to within 1% accuracy. Moreover, the temperature differences that drive the thermal stresses ($\Delta T_{\text{panel}}=(\Delta T_{\text{panel}}^c+\Delta T_{\text{panel}}^w)/2$ and $\Delta T_{tf}=\Delta T_{tf}^c$, see Appendix B for details) are also predicted adequately (within about 8%). FE calculations for other panel designs and material properties yielded similar consistency between the numerical results and analytic predictions.

Table 1 Approximate chemical compositions of the candidate metallic alloys

Material	Approximate chemical composition (wt %)
Inconel 625	Ni–20% Cr–10% Mo–5% Fe–3% Nb
Inconel X-750	Ni–15% Cr–7% Fe–2.5% Ti
Ti 6Al 4V	Ti–6% Al–4% V
Ti β 21S	Ti–15% Mo–2.7% Nb–3% Al–0.2% Si
NARloy-Z	Cu–3% Ag–0.5% Zr
GRCop-84	Cu–6.5% Cr–5.8% Nb
Nb-Cb752	Nb–10% W–2.5% Zr

4 Stress Distributions

Stress estimates were obtained using standard concepts of plate bending and stretching and assuming the materials to be linear elastic. Derivations and solutions are in Appendix B. In practice, some nonlinearity may occur in the most highly stressed locations, enabling stress redistribution and shakedown [15,16]. Conse-

Table 2 Thermal and mechanical properties of the candidate materials

Material	T^* (K)	σ_Y (T_f^0) (MPa)	$d\sigma_Y/dT$ (MPa/K)	E (GPa)	CTE (10^{-6}/K)	k_s (W/m K)	ρ_s (kg/m^3)
Inconel 625	1100	427	−0.31	164	14.0	20.0	8440
Inconel X-750	1100	795	−0.39	128	16.0	23.0	8276
Ti–6Al–4V	675	909	−0.83	90	10.0	11.0	4430
Ti-β-21S	815	1222	−1.46	100	10.3	21.0	4940
NARloy-Z	811	99	−0.009	125	17.0	350.0	9130
GRCop-84	973	205	−0.18	90	19.0	285.0	8756
Nb–Cb752	1470	382	−0.17	110	7.4	50.0	9030
SiC–SiC	1640	200	—	240	4.1	25(∥), 20 (⊥)	2900
C–SiC	1810	200	—	100	2.0	15(∥), 5 (⊥)	2000
TBC (ZrO_2)						1.0	3000

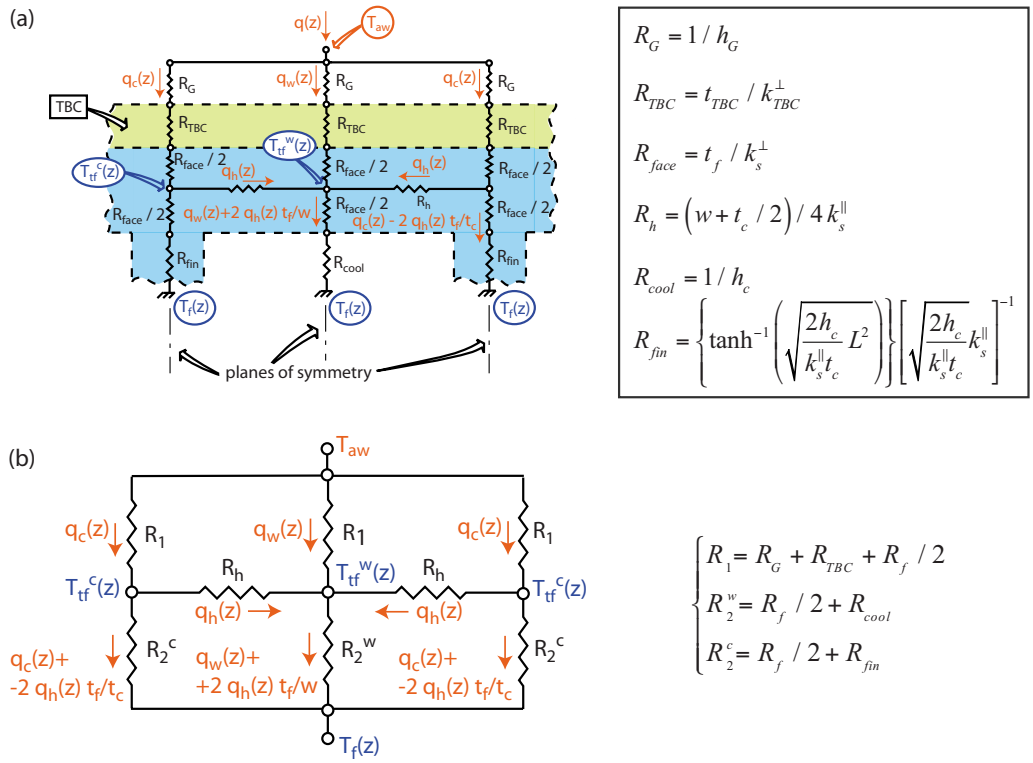

Fig. 3 (*a*) **Thermal resistance network used to determine temperature distributions, along with expressions for all relevant thermal resistances.** (*b*) **Effective network.**

quently, in the absence of high cycle fatigue, the ensuing results are conservative. A subsequent article will incorporate yielding and shakedown and provide an assessment of the extent of the conservatism. Although the present analysis is for a flat panel, its extension to cylindrical configurations is straightforward.

4.1 Boundary Conditions. Two idealized sets of boundary conditions are considered.

I. Linear frictionless supports along the edges in the z-direction (Fig.6(a)). This constraint prevents bending in the z-direction, while allowing it in the x-direction (albeit with no rotation at the ends). Uniform thermal expansion is allowed along all directions. The analog for a cylinder would be the absence of constraint on

Table 3 Physical properties of JP-7 jet fuel

Fuel	k_f (W/m K)	μ_f (Pa s)	c_p (J/kg K)	Pr_f	ρ_f (kg/m^3)	T_{coke} (K)
JP-7	0.11	1.984×10^{-4}	2575	4.64	800	975

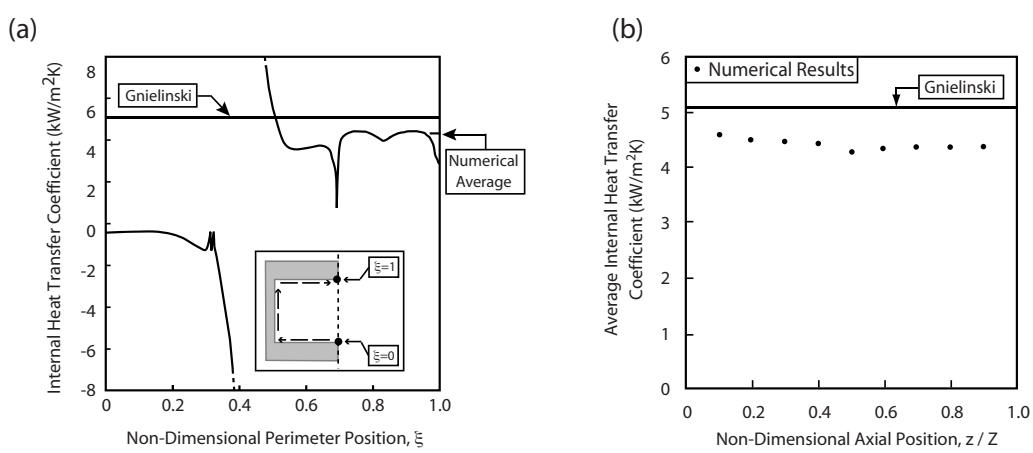

Fig. 4 Distribution of the heat transfer coefficient in the cooling channel extracted from the CFD simulation of a near-optimal Inconel X-750 panel. (*a*) **Variation of pointwise h_C around channel perimeter at $z/Z=0.9$.** (*b*) **Variation of cross-section averaged h_C along the axial direction. The value extracted from the Gnielinski correlation (Eq. (A1)) and used in the analytical model is depicted for comparison.**

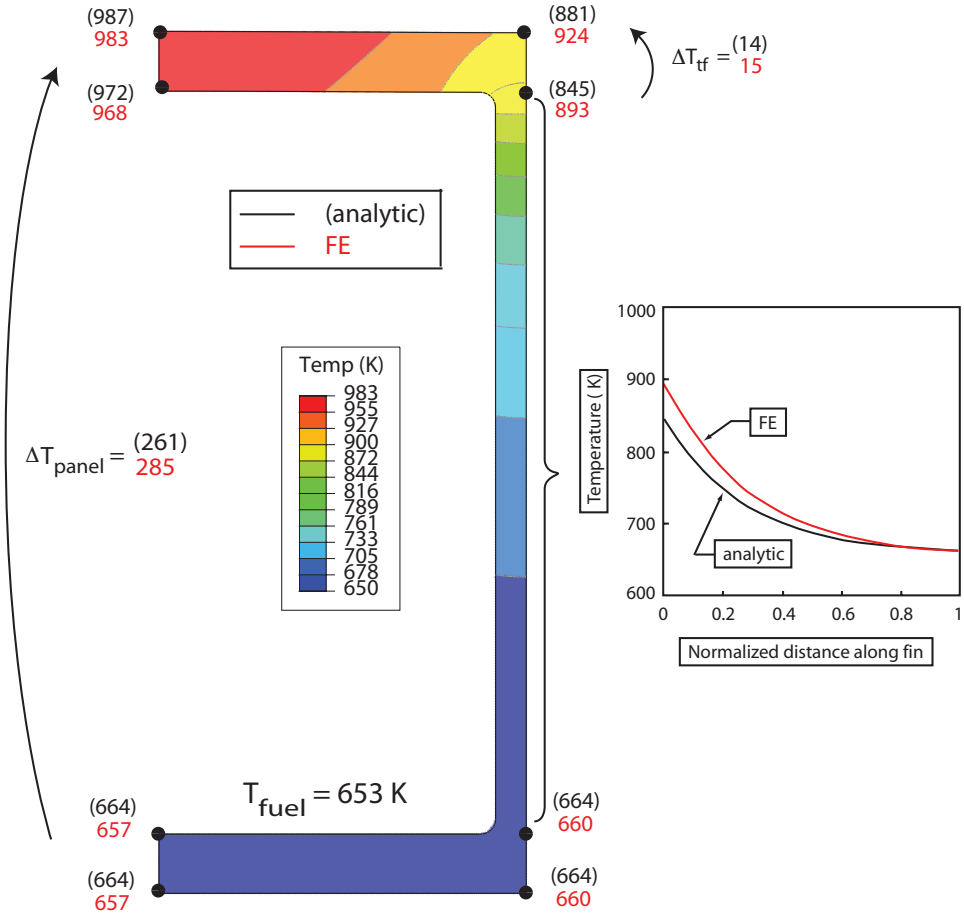

Fig. 5 Comparison of analytical and numerical (FE) temperature distributions for an optimal Inconel X-750 panel. All temperatures are in Kelvin. Values in parentheses are analytical predictions. Both the maximum temperature in the structure and the temperature differences that drive the thermal stresses are captured accurately.

changes in both the diameter and axial length. This boundary condition can also represent *multiple* linear frictionless supports (Fig. 6(*b*)) by simply re-interpreting the panel width b as the support spacing.

II. Two-dimensional continuous bed of rollers (Fig. 6(c)). Uniform thermal expansion is permitted in all directions. The external pressure does not cause panel-level bending but the internal pressure can bend individual face segments.

The use of rollers instead of frictional supports allows uniform thermal expansion of the panel (with no bending). While the practical implementation may be challenging, attaining these conditions is essential to viable solutions. Otherwise, if the plate is clamped on all sides, the maximum temperature increase that can be sustained without yielding is only $\Delta T_{\max}=(1-\nu)\sigma_Y/E\alpha$ (with E being Young's modulus, α the thermal expansion coefficient, σ_Y the material yield strength, and ν Poisson's ratio) [17], well below the upper use temperature of all of the materials (Fig. 6(*d*)).

Both the pressure drop and the temperature variation along the panel length have been neglected. This assumption, combined with the imposed boundary conditions, ensures that generalized plane strain conditions are attained along the z-direction.

4.2 Failure Locations. Although the temperature differences, and hence the thermal stresses, are greatest at the channel inlet, the material strength is also greatest at this location. Typical strength reductions with increasing temperature suggest the possibility of preferential failure at the outlet, where the temperature is at its maximum. To ensure accurate prediction of failure initiation, thermal stresses should be ascertained at *each cross section* and compared with material strength at the pertinent (local) temperature. Additionally, the stresses due to pressure loads vary with location within the same cross section and can be of opposite sign relative to those caused by thermal loads. Thus, establishing a priori the failure location is not straightforward.

To address this problem, a set of 18 "critical points" has been identified for close scrutiny, clustered around two failure-susceptible channels: one at the periphery closest to the supports and the other at the center (Fig. 7). Failure of the structure is averted provided that, for metallic alloys, the Mises stress at each point remains below the elastic limit. The analog for CMCs is based on a maximum or minimum principal stress criterion. The internal pressure in the core channels (which induces large tensile stresses in all members) combined with the relatively stubby shape of the optimized members make it unnecessary to design against buckling [18–26].

The accuracy of the stress predictions was verified by FE calculations. Illustrative results are presented for the optimized Inconel X-750 panel subject to the thermal loads described in the preceding section. The calculations use type II boundary conditions and an internal fuel pressure of 4 MPa (The pressure in the combustion chamber can be neglected since it has minimal effect on the stresses for the selected boundary condition.) The bottom is constrained against translation in the y-direction and periodic boundary conditions are imposed on the vertical sides (one side is constrained against translation in the x-direction, whereas all nodes on the other are required to displace equally in the x-direction). The top is traction free.

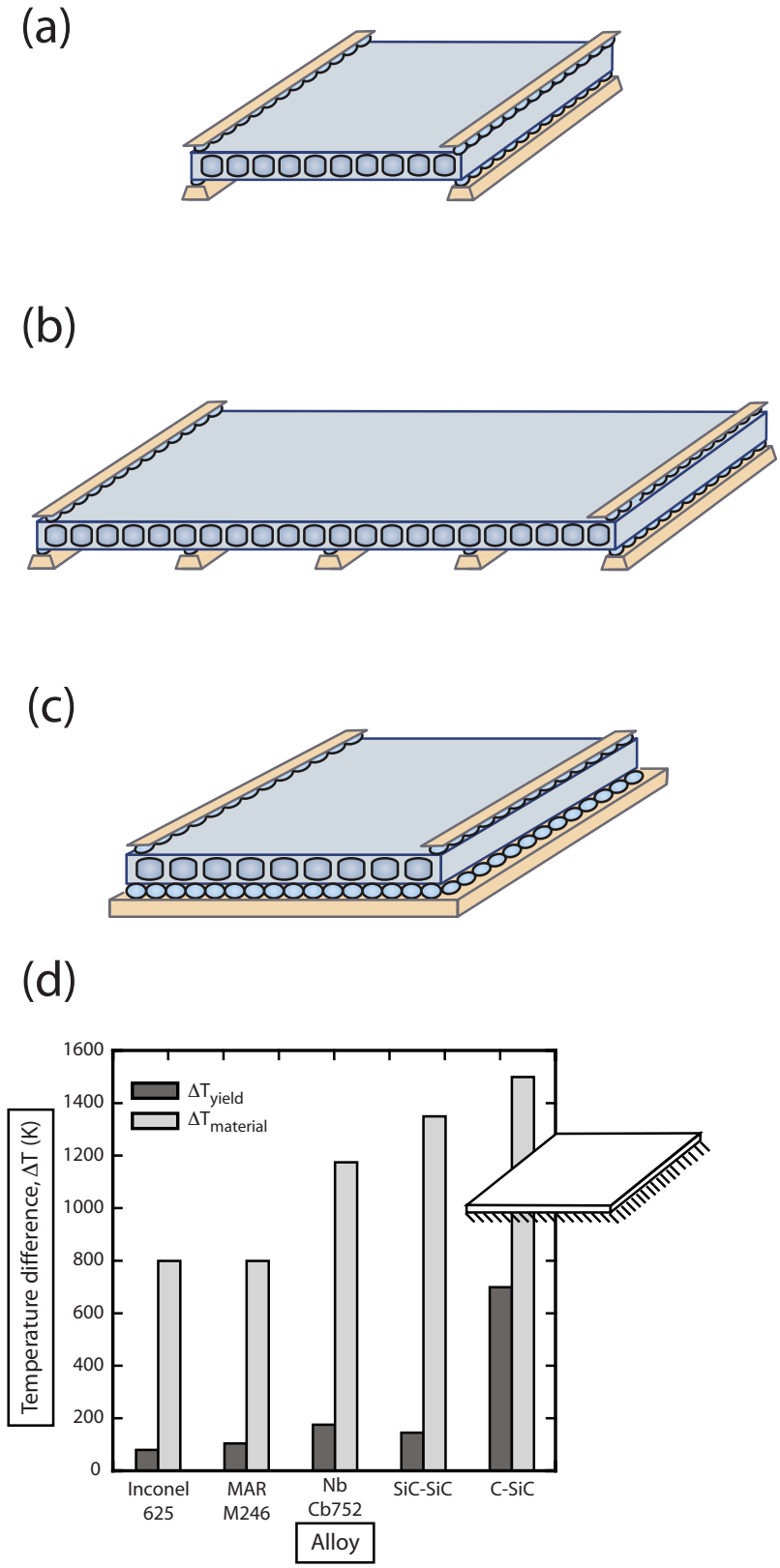

Fig. 6 Mechanical boundary conditions. [(*a*) and (*b*)] **Linear rollers on two sides (Type I). (*b*) Multiple linear rollers with regular spacing. (*c*) Uniform two-dimensional bed of rollers, with impeded rotation at the ends (Type II). (*d*) Benchmark boundary condition: plate sitting on rigid foundation (inset). The chart compares the temperature increase from room temperature to the material upper use limit needed to cause yielding. Under this boundary condition, the full high-temperature potential of the materials is not exploited.**

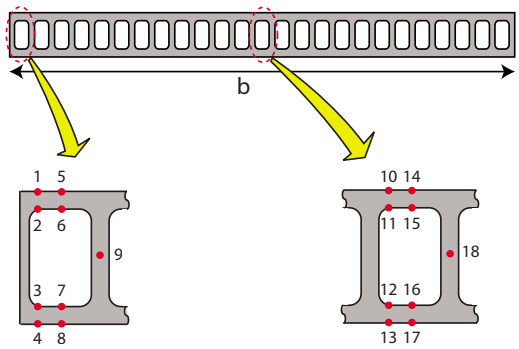

Fig. 7 Unit cells susceptible to local yielding and the 18 critical points

The resulting distribution in the Mises stress is plotted on Fig. 8. Also shown are comparisons between the numerical results and the analytic predictions along the four critical trajectories, corresponding to the external and internal surfaces of both face sheets, for thermal, mechanical, and combined thermomechanical loadings. The analytic prediction is accurate to within 1% at the most highly stressed location (Point 1) and within ~10% at other locations on the top face. The corners (Point 2), where stress intensification is evident, are exceptions. This discrepancy has not been pursued for several reasons. (i) For this particular simulation, because of the relatively low temperature at the corners (Fig. 5), the yield strength is high (Table 2) and, given the stress distribution (Fig. 8), both corners remain elastic. We speculate that this concept generalizes to metallic systems, but a formal proof requires further analysis. (ii) Even if localized plasticity at the corners could not be avoided, the metallics can be readily designed to assure shakedown, wherein local plasticity occurs only during the first few thermomechanical cycles. Such a solution may not be possible for CMCs. (iii) The stress intensification can be reduced by increasing the fillet radius without imposing a significant weight penalty.

The agreement on the bottom face is somewhat worse (~20% at Point 3). This result is implicit in the model, which underestimates the thermal stress in the bottom face to ensure conservative stress estimates on the top face. This choice was made because the critical condition (yielding or fracture) typically occurs in the top face. Comparisons performed for other materials and geometries showed similar correlations.

The numerical calculations confirm that the combined thermomechanical stresses are not necessarily the most dangerous. At Point 5, for instance, the thermal stresses alone are greater than those under thermomechanical loading.

5 Materials Selection for Scramjet Combustor Liners

The materials selection procedure exposed in Sec. 2 is applied to the combustor liner of a Mach 7 scramjet cruise vehicle operating with JP-7 jet fuel. The choice is motivated by the realization

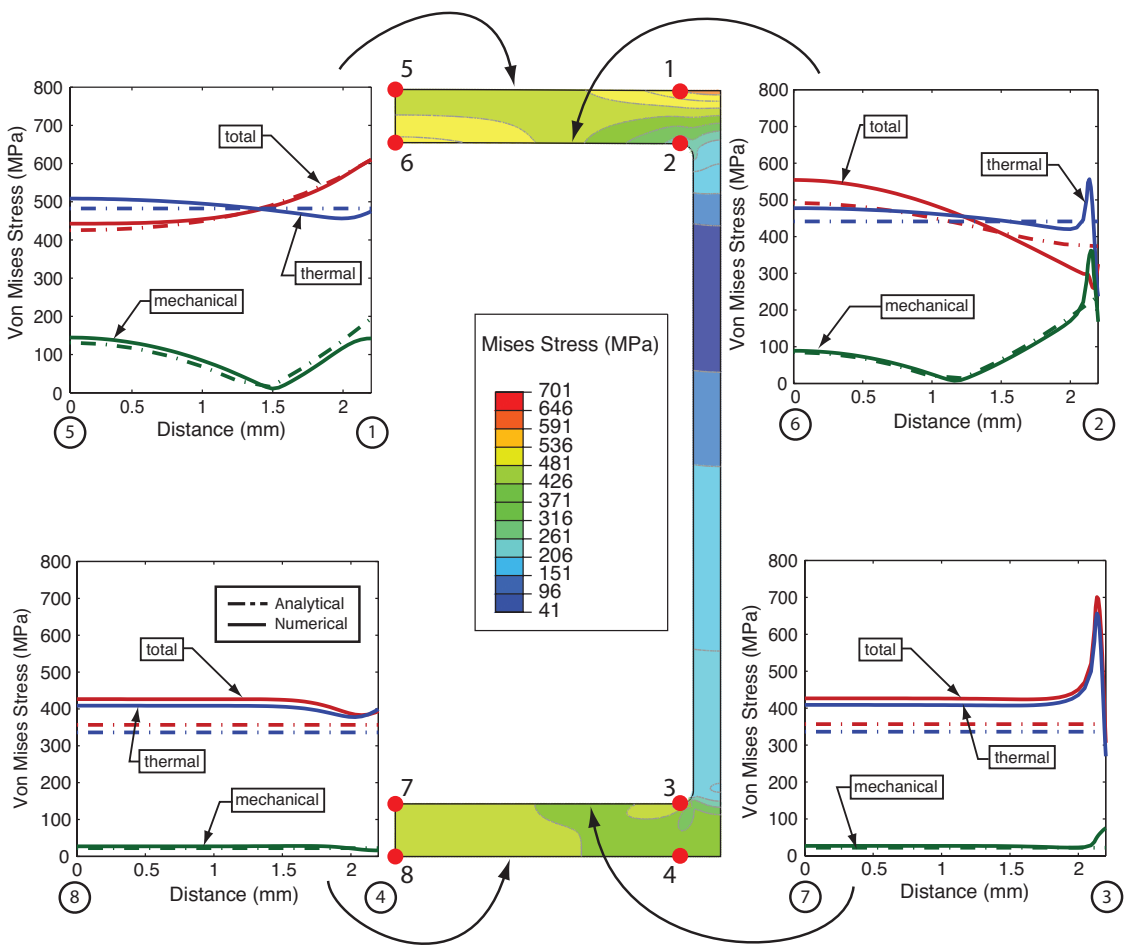

Fig. 8 Comparison of analytical and numerical (FE) von Mises stress distributions for an optimal Inconel X-750 panel. The plots show the results for thermal, mechanical, and combined thermomechanical stresses along the four paths. With the exception of Points 2 and 3, clearly affected by stress intensification, the agreement is satisfactory, particularly on the top face, where the highest stresses generally occur.

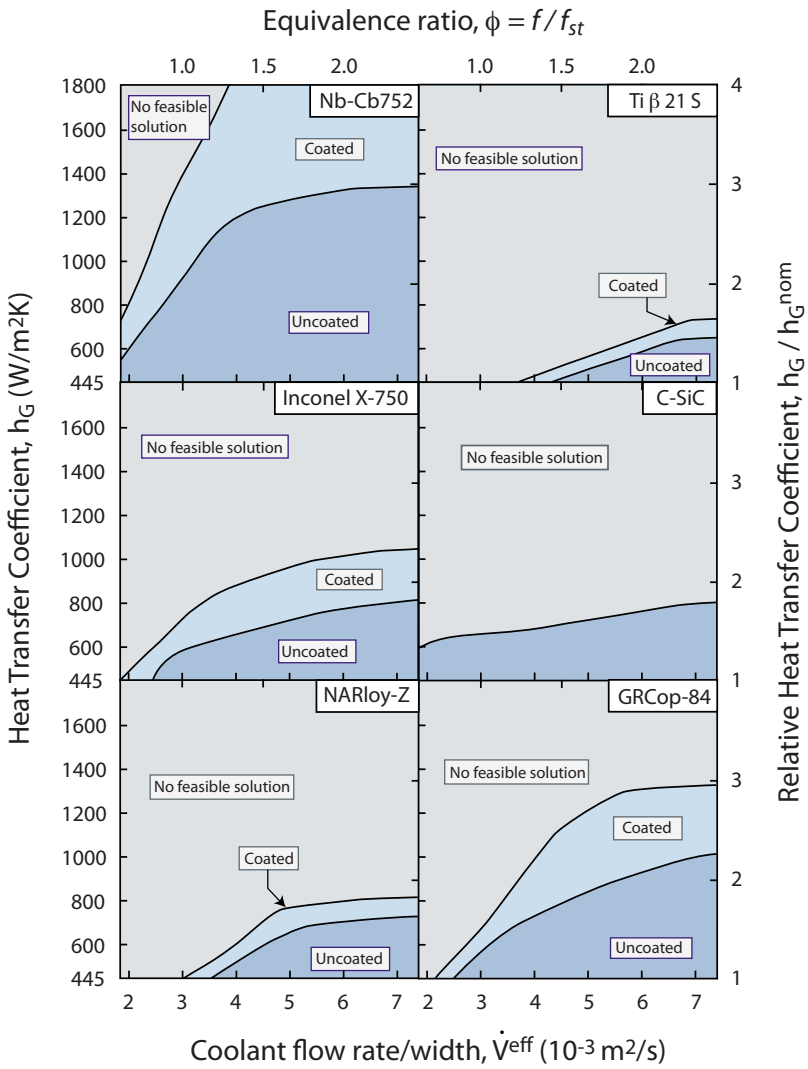

Fig. 9 Design maps for several materials considered in this study, with and without a TBC. The normalizing parameters for the equivalence ratio ($\phi = f/f_{st}$) and the heat transfer coefficient (h_G/h_G^{nom}) are those expected for steady-state Mach 7 flight conditions.

that the design of vehicles in this velocity range is most mature and in urgent need of technological advancements in high-temperature materials and structures.

5.1 Thermomechanical Loads. The thermomechanical loads on the combustor liners depend on nearly every aspect of the vehicle design, including the size and shape of the compression ramp, the size of the combustion chamber, details of the injection system, and combustion efficiency. For the present illustration, the vehicle is assumed to be 10 m long and 2.5 m tall, with a bilinear compression ramp that generates three oblique shocks. The pertinent aerothermodynamic conditions for the prescribed vehicle velocity and optimal flight altitude are detailed in Ref. [3]. Fuel enters the cooling channels with pressure $p_f^o = 4$MPa and initial temperature $T_f^o = 400$ K. On the combustion side, the pressure $p_{comb} = 0.16$ MPa, the adiabatic wall temperature $T_{aw} = 3050$ K and the heat transfer coefficient $h_G = 445$ W/m^2 K. To assess the effects of potential heat spikes in the combustion chamber, heat transfer coefficients up to 1800 W/m^2 K are considered. For the stress analysis, Type I boundary conditions are used with an unsupported span, $b = 0.5$ m.

For stoichiometric combustion, the fuel flow rate (per unit width of combustor) is $\dot{V}_{st} = 0.008$ m^2/s. Since the total perimeter of the combustor liner is $2(b + H_{comb})$, with H_{comb} the height of the chamber, the effective flow rate per unit width of liner is $\dot{V}_{st}^{eff} = \dot{V}_{st} b / 2(b + H_{comb})$. Upon specifying the dimensions ($b = 0.5$ m and $H_{comb} = 15$ cm), then $\dot{V}_{st}^{eff} = 0.003$ m^2/s. To address offstoichiometric combustion, an equivalence ratio ϕ is introduced, defined by $\phi = f/f_{st}$, where f is the actual fuel-to-air mass ratio and f_{st} is the corresponding stoichiometric value. The actual flow rate then becomes $\dot{V}^{eff} = \phi \dot{V}_{st}^{eff}$. The range $0.6 < \phi < 2.5$ is used for subsequent calculations.

5.2 Design Constraints. A candidate design is deemed acceptable provided it satisfies four principal constraints: (i) the stresses induced by the pressure and the thermal loads remain below representative levels of material strength, σ_Y; (ii) the maximum material temperature T_m^{max} does not exceed the upper use limit, T^*; (iii) the fuel temperature remains below that for coking ($T_{coke} = 975$ K [27]); and (iv) the pressure drop through the channels is acceptably low ($\Delta p \leq 0.1$ MPa). Additionally, to ensure that designs can be manufactured, secondary constraints are imposed on some dimensions, notably: channel width $w \geq 2$ mm, channel height $L \geq 5$ mm, face and core wall thicknesses t_c and $t_f \geq 0.4$ mm, and TBC thickness ≤ 0.3 mm.

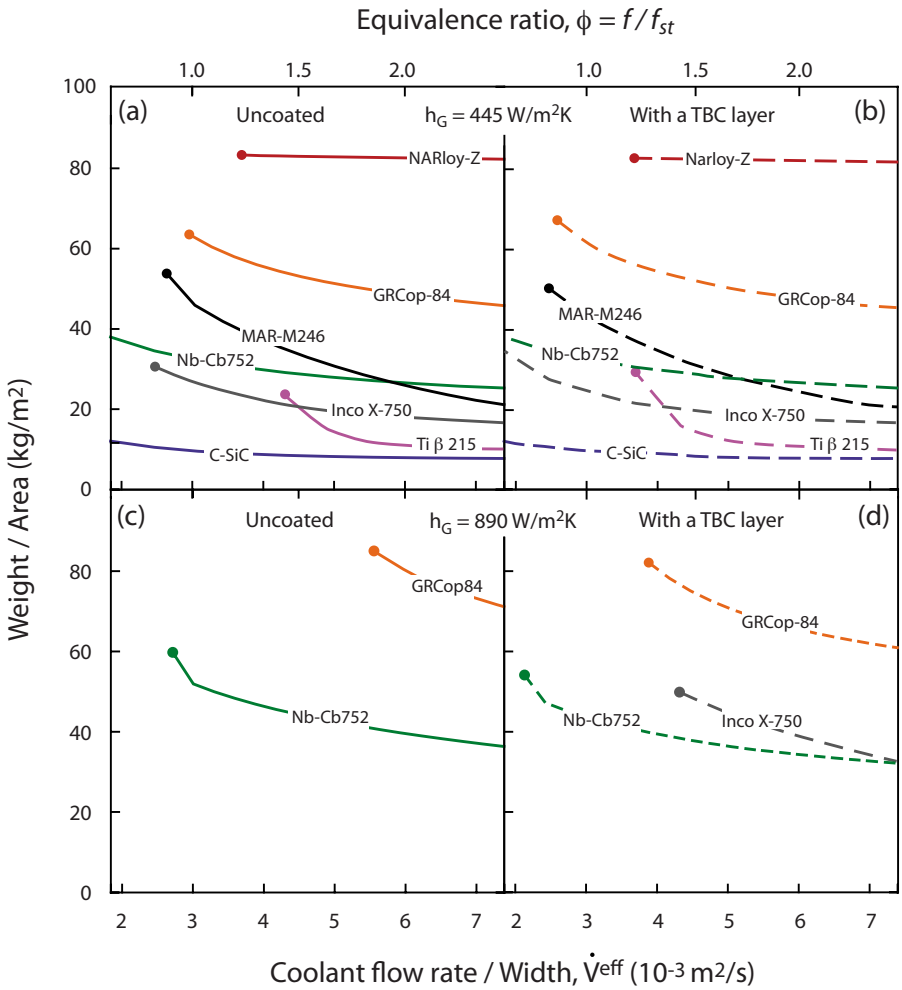

Fig. 10 Minimum weight comparison at two levels of heat transfer: (*a*) and (*b*) h_G=445 and (*c*) and (*d*) 890 W/m^2 K. [(*a*) and (*c*)] the solid lines represent the results for uncoated materials whereas [(*b*) and (*d*)] the dashed lines are those for TBC coated materials.

For metallic alloys, the yield strength is assumed to decrease linearly with temperature for $T \leq T^*$. For the CMCs, the tensile and compressive strengths are assumed equal and independent of temperature. Caveats on this choice are discussed later.

5.3 Optimization Scheme. Whenever a solution exists, the design was optimized for minimum weight. The mass of the TBC is included to ensure that a finite layer emerges only if it reduces the overall weight. Numerical optimizations were performed using the quadratic optimizer MINCON in MATLAB™. Several randomly generated initial guesses were used to escape from local minima. In some cases, a manual optimization scheme was employed to verify the accuracy of the numerical results.

5.4 Principal Results and Interpretation. The procedure was implemented for a suite of high-temperature materials. Approximate chemical compositions of the candidate metallic alloys are listed in Table 1; relevant mechanical properties (for metallic and ceramic systems) are summarized in Table 2. Design maps are presented in two formats. (i) In the first (Fig. 9), the ordinate is h_G, motivated by the appreciation that shocks passing through the combustor can cause local elevations. The abscissa is the fuel flow rate, $\dot{V}^{\text{eff}}$. The normalizing parameters for the equivalence ratio ($\phi = f/f_{\text{st}}$) and the heat transfer coefficient (h_G/h_G^{nom}) are those expected for steady-state Mach 7 flight conditions. The map specifies domains within which the material can function, with and without a TBC, as well as a domain of inadmissibility. In this scheme, the weight is a function of the location on the map. (ii) In the second (Fig. 10), h_G is fixed (at either 445 W/m^2 K or 890 W/m^2 K), the ordinate is the weight of the optimized panel and the abscissa is again the fuel flow rate.

The overarching implications from Fig. 9 are as follows. (i) In all cases where solutions are obtained, increasing the flow rate is beneficial, indicating that the cooling efficiency limits the design (as opposed to the fuel pressure drop). (ii) Among the selected materials, most provide a solution for the nominal Mach 7 conditions (h_G=445 W/m^2 K). The exceptions are Inconel 625, Ti–6Al–4V, and SiC–SiC, which are *not viable* anywhere within the design space. (iii) The outcome changes radically if the heat load is doubled. Namely, for h_G=890 W/m^2 K, only the Nb alloy Cb752 and the Cu alloy GRCop-84 are viable without a TBC (albeit an environmental barrier coating will be needed to avert oxidation [28]). Furthermore, Cb752 is the only material that can survive without a TBC at near-stoichiometric fuel flow rates (ϕ =1). (iv) The operational design space of essentially all metallics can be increased by using a TBC, although the benefit differs among materials: Cb752, Inconel X-750, and GRCop-84 showing the largest advantage.

Figure 10 compares the optimal panel weights for cases with and without a TBC. For h_G=445 W/m^2 K, C–SiC offers the lightest structure (by a factor greater than 2 relative to most metallic

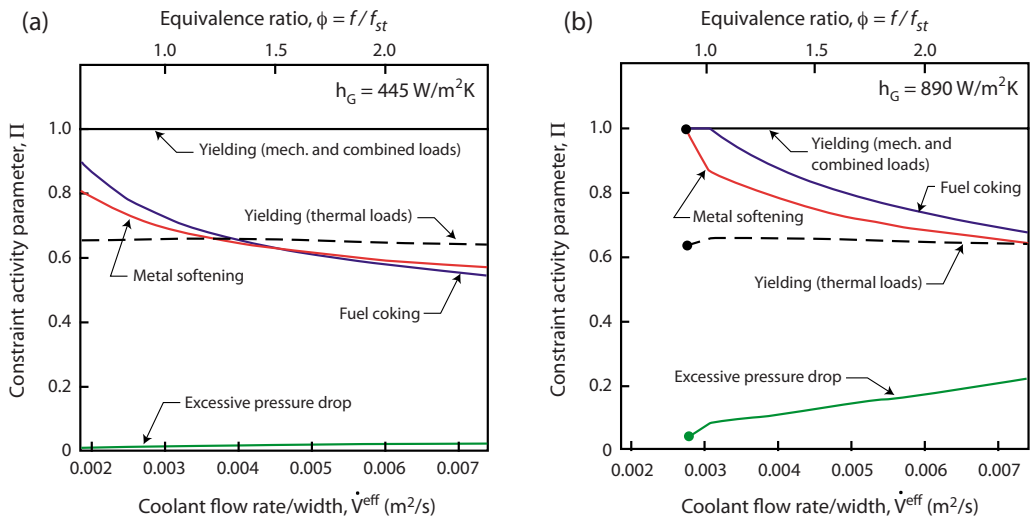

Fig. 11 Constraint activity map for Cb752 for h_G values of (a) 445 W/m^2 K and (*b*) 890 W/m^2 K. Constraint is active when its activity parameter reaches unity. At the lower thermal load, only the therm-omechanical constraints are active (yielding under mechanical and combined loads). When the thermal load is doubled, at low flow rates, both the solid and fuel temperatures approach their maximum allowable value.

alloys), followed by Inconel X-750 and Cb752. Ti-β21S provides a lightweight alternative but only when high fuel flow rates are permitted. For h_G=890 W/m^2 K, the only viable uncoated materials are Cb752 and GRCop-84. However, these two materials exhibit vastly different weight efficiencies: Cb752 is half the weight of GRCop-84. When a TBC is used, the selection is expanded to include Inconel X-750. (Perhaps surprisingly, C–SiC is not viable at this heat flux, with or without a TBC, because both the thermal and the pressure-induced stresses on the hot face exceed its compressive strength). A caveat to this outcome is discussed below. Although a TBC on the Cb752 would enable a slightly lighter structure, its use would be predicated on the tradeoff between weight savings and added cost. Finally, while increasing the fuel flow rate generally results in lighter structures, the weight savings is unlikely to be significant enough to overcome the weight penalty associated with the extra fuel.

The design maps of Fig. 9 and the weight analysis of Fig. 10 do not divulge the significant amount of valuable information contained in the code about optimal geometries, temperatures, stresses, and the relative importance of the various design constraints. Complete description of these results is beyond the scope of this paper but will be presented in subsequent more detailed assessments. One notable observation is that, for essentially all of the materials and design space, the thermomechanical constraint is always active. That is, the design is limited by the occurrence of yielding or fracture. This feature is illustrated for Cb752 in Fig. 11, expressed in terms of constraint activity parameters, Π (defined in such a way that unity signals activation of the constraint). Occasionally, other constraints are also active. For example, at low fuel flow rates and high heat flux, the maximum temperatures in both the structure and the fluid reach their allowable limits.

6 Conclusions

A materials selection strategy has been presented for actively cooled panels, with implications for aerospace structures. The procedure encompasses a geometry optimization tool coupled with analytical models for temperatures and thermomechanical stresses. A thermal network approach has been used to derive the temperature distribution, accounting for the possible presence of a TBC. A sandwich panel analysis has been adopted for the thermomechanical stress calculations. The accuracy of the model predictions and the underlying assumptions has been verified numerically, employing a combination of FE and CFD calculations.

The methodology has been applied to the combustor liner of a Mach 7 hydrocarbon-powered vehicle. Realistic operating conditions have been estimated based on established aerothermodynamics considerations [3]. Many of the candidate materials present feasible designs for at least a limited range of operating loads, representative of steady-state flight conditions and stoichiometric fuel combustion. However, the suite of material options is sensitive to the operating loads and the permitted fuel flow rate. In the present illustration, only Cb752 is viable at the highest heat load and under stoichiometric fuel combustion. This result, combined with robustness benefits and fabrication facility, emphasizes its potential for superior performance, subject to the proviso that oxidation is averted through the use of environmental barrier coatings. For higher fuel flow rates and/or the addition of a TBC, GRCop-84 and Inconel X-750 become viable, although Cb752 remains the most weight efficient.

Finally, since the thermomechanical constraint is almost always active in the optimized designs, elevations in the high-temperature strength of the candidate alloys would yield direct benefits in weight efficiency. Furthermore, based on observations that C–SiC can sustain larger temperature gradients than the present model assumes [29], it should re-emerge as a viable candidate for the more severe thermal environments once a revised local-basis failure criterion has been established.

Acknowledgment

This work was supported by the ONR through a MURI program on Revolutionary Materials for Hypersonic Flight (Contract No. N00014-05-1-0439). The authors are thankful to David Marshall of Teledyne, and Thomas A. Jackson and William M. Roquemore of AFRL for insightful discussions.

Nomenclature

A_f = cross-sectional area of the face in a unit cell (m^2)
A_c = cross-sectional area of the core web in a unit cell (m^2)
b = combustor width (m)
$c_{p,f}$ = specific heat of the coolant (J/kg K)

D_h = hydraulic diameter of the cooling ducts (m)
E = Young's modulus (Pa)
f = friction factor
ϕ = fuel/air mass ratio
f_{st} = stoichiometric fuel/air mass ratio
H = panel thickness (m)
H_{comb} = combustion chamber height (m)
h_G = heat transfer coefficient on the combustor side ($W/m^2\,K$)
h_G^{nom} = heat transfer coefficient on the combustor side for a notional Mach 7 vehicle ($W/m^2\,K$)
h_C = heat transfer coefficient on the cooling channel walls ($W/m^2\,K$)
$k_s^{\perp}$ = through-thickness thermal conductivity of the material (W/m K)
$k_s^{\parallel}$ = in-plane thermal conductivity of the material (W/m K)
k_f = thermal conductivity of the coolant (W/m K)
k_{TBC} = through-thickness thermal conductivity of the TBC (W/m K)
L = height of cooling channel (m)
p_f = pressure in the coolant (Pa)
p_f^0 = entry pressure in the coolant (Pa)
p_{comb} = pressure in the combustion chamber (Pa)
Pr = Prandtl number
q_w = heat flux into the web (W/m^2)
q_c = heat flux convected from the top face into the coolant (W/m^2)
q_h = horizontal heat flux in the top face (W/m^2)
R_G = external convective thermal resistance $(W/m^2\,K)^{-1}$
R_{cool} = internal convective thermal resistance $(W/m^2\,K)^{-1}$
R_{TBC} = conductive thermal resistance across the TBC $(W/m^2\,K)^{-1}$
R_{face} = conductive thermal resistance across the top face $(W/m^2\,K)^{-1}$
R_h = conductive thermal resistance along the top face $(W/m^2\,K)^{-1}$
R_1, R_2^w, R_2^c = combination of thermal resistances $(W/m^2\,K)^{-1}$
R_w^*, R_c^*, R_h^* = non-dimensional combination of thermal resistances
Re = Reynolds number
T_{aw} = adiabatic wall temperature in the combustor (K)
T_f = coolant temperature (K)
T_f^0 = entry coolant temperature (K)
T_f^{max} = maximum coolant temperature (K)
T_m^{max} = maximum temperature in the material (K)
T_{tf}^w = temperature on the top side of the top face, over a web (K)
T_{tf}^c = temperature on the top side of the top face away from a web (K)
$T^{(i)}$ = temperature at a location i in the material (K)
T^* = maximum allowable temperature in the material (K)
T_{coke} = coking temperature of the coolant (K)
t_f = face sheet thickness (m)
t_c = core web thickness (m)
u = coolant velocity (m/s)
$\dot{V}^{eff}$ = volumetric fuel flow rate per unit width of the panel (m^2/s)
$\dot{V}_{st}$ = stoichiometric volumetric fuel flow rate per unit width of the combustor (m^2/s)
$\dot{V}_{st}^{eff}$ = stoichiometric volumetric fuel flow rate per unit width of the panel (m^2/s)
w = width of cooling channel (m)
Z = panel length (m)
α = coefficient of thermal expansion of the material (K^{-1})
Δp = viscous pressure drop across the panel (Pa)
ΔT_{panel}^c = temperature difference across the panel away from the core web (K)
ΔT_{panel}^w = temperature difference across the panel above a core web (K)
ΔT_{panel} = relevant temperature difference across the panel (K)
ΔT_{tf}^c = temperature difference across the top face away from the core web (K)
ΔT_{tf}^w = temperature difference across the top face above a core web (K)
ΔT_{tf} = relevant temperature difference across the top face (K)
x, y, z = geometric coordinates
ϕ = equivalence ratio
ν_f = kinematic viscosity of the coolant (m^2/s)
υ = Poisson's ratio of the material
σ_Y = yield strength of a metallic material (Pa)
σ_{ult} = ultimate stress for a CMC (Pa)
$\sigma_{core,y}^{p_f}$ = stress in the core web along the y-direction due to the pressure p_f (Pa)
$\sigma_{core,z}^{p_f}$ = stress in the core web along the z-direction due to the pressure p_f (Pa)
$\sigma_{face,x}^{p_f}$ = stress in the face sheet along the x-direction due to the pressure p_f (Pa)
$\sigma_{face,z}^{p_f}$ = stress in the face sheet along the z-direction due to the pressure p_f (Pa)
$\sigma_{face,x}^{p_{comb}}$ = stress in the face sheet along the x-direction due to the pressure p_{comb} (Pa)
$\sigma_{face,z}^{p_{comb}}$ = stress in the face sheet along the z-direction due to the pressure p_{comb} (Pa)
$\sigma_{face,x}^{\Delta T_{panel}}$ = stress in the face sheet along the x-direction due to the temperature difference ΔT_{panel} (Pa)
$\sigma_{face,z}^{\Delta T_{panel}}$ = stress in the face sheet along the z-direction due to the temperature difference ΔT_{panel} (Pa)
$\sigma_{face,x}^{\Delta T_{tf}}$ = stress in the face sheet along the x-direction due to the temperature difference ΔT_{tf} (Pa)
$\sigma_{face,z}^{\Delta T_{tf}}$ = stress in the face sheet along the z-direction due to the temperature difference ΔT_{tf} (Pa)
$\sigma_{m,x}^{(i)}$ = mechanical stress at location i along the x-direction (Pa)
$\sigma_{m,z}^{(i)}$ = mechanical stress at location i along the z-direction (Pa)
$\sigma_{T,z}^{(i)}$ = thermal stress at location i along the x-direction (Pa)
$\sigma_{T,x}^{(i)}$ = thermal stress at location i along the z-direction (Pa)
ρ_f = mass density of the coolant (kg/m^3)
θ = nondimensional fin temperature: $(T(y)-T_{fuel})/(T(0)-T_{fuel})$

Appendix A: Thermal Resistance Model

The Model

Among the nine thermal resistances in the model network (Fig. 3(*a*)), six are independent:

- top face/hot gas boundary: $R_G = 1/h_G$
- across TBC (when present): $R_{\mathrm{TBC}} = t_{\mathrm{TBC}}/k_{\mathrm{TBC}}^{\perp}$
- across hot face (y-direction): $R_{\mathrm{face}} = t_f/k_s^{\perp}$
- along hot face (x-direction)[1]: $R_h = (w + t_c/2)/4k_s^{\parallel}$
- top face/coolant boundary: $R_{\mathrm{cool}} = 1/h_c$
- core web (modeled as a 1D thermal fin [30,31]): $R_{\mathrm{fin}} = \{\tanh^{-1}(\sqrt{2h_C/k_s^{\parallel}t_c L^2})\}[\sqrt{2h_C/k_s^{\parallel}t_c k_s^{\parallel}}]^{-1}$.

Here, h_G and h_C are the heat transfer coefficients on the hot gas side and coolant sides, respectively; $k_s^{\perp}$ and $k_s^{\parallel}$ are the through-thickness and in-plane thermal conductivities of the material (the distinction being important for CMCs, wherein $k_s^{\perp} \ll k_s^{\parallel}$); and k_{TBC} is the through-thickness conductivity of the TBC (its in-plane value is taken as zero, due to the columnar structure of coatings produced by physical vapor deposition).

Assuming flow in the cooling channels is turbulent and fully developed, h_C is given by the Gnielinski correlation [14,32]:

$$h_C = \frac{k_f}{D_h}\mathrm{Nu} = \frac{k_f}{D_h}\frac{(f/2)(\mathrm{Re}-1000)\mathrm{Pr}}{1 + 12.7\sqrt{f/2}(\mathrm{Pr}^{2/3}-1)} \tag{A1}$$

where k_f is the thermal conductivity of the coolant, Pr is the Prandtl number, $D_h = 2wL/(w+L)$ is the hydraulic diameter, and Re is the Reynolds number:

$$\mathrm{Re} \equiv \frac{uD_h}{\nu_f} = \frac{\dot{V}^{\mathrm{eff}} D_h H(w+t_c)}{LwH\nu_f} \tag{A2}$$

with ν_f being the kinematic viscosity, $\dot{V}^{\mathrm{eff}}$ the volumetric flow rate per unit width of panel (see Sec. 5.2), and f is the friction factor, given by $f = 0.046\mathrm{Re}^{-1/5}$ in the domain $2\times10^4 < \mathrm{Re} < 10^6$ [32,33].

[1]The horizontal resistance is not properly conductive, as convection occurs along one of the sides. FE calculations reveal that using an effective length equal to half the actual length yields accurate results (hence the factor of 4).

The model can be simplified into the effective network of Fig. 3(b), characterized by four resistances, R_1, R_2^w, R_2^c, R_h, where

$$R_1 = R_G + R_{\mathrm{TBC}} + R_f/2$$

$$R_2^w = R_f/2 + R_{\mathrm{cool}}$$

$$R_2^c = R_f/2 + R_{\mathrm{fin}} \tag{A3}$$

(with R_h previously defined). The temperatures of interest are those on the top face, directly over (T_{tf}^c) and midway between (T_{tf}^w) the core members, at both the inlet ($z=0$) and the outlet ($z=Z$). Since the three fluxes q_w, q_c, q_h are also unknown, five equations are needed to close the system:

$$T_{\mathrm{aw}} - T_{\mathrm{fuel}} = q_w R_1 + (q_w + 2q_h t_f/w)R_2^w$$

$$T_{\mathrm{aw}} - T_{\mathrm{fuel}} = q_c R_1 + (q_c - 2q_h t_f/t_c)R_2^c$$

$$T_{\mathrm{aw}} - T_{tf}^w = q_w R_1$$

$$T_{\mathrm{aw}} - T_{tf}^c = q_c R_1$$

$$T_{tf}^c - T_{tf}^w = q_h R_h \tag{A4}$$

The solution gives the heat fluxes:

$$q_c = \frac{T_{\mathrm{aw}} - T_f}{R_1}R_c^*$$

$$q_w = \frac{T_{\mathrm{aw}} - T_f}{R_1}R_w^*$$

$$q_h = \frac{T_{\mathrm{aw}} - T_f}{R_1}R_h^* \tag{A5}$$

where

$$R_w^* = \frac{R_1[R_2^c R_h + R_1(R_h + 2R_2^c t_f/t_c + 2R_2^w t_f/w)]}{R_2^c R_2^w R_h + R_1{}^2(R_h + 2R_2^c t_f/t_c + 2R_2^w t_f/w) + R_1\{R_2^w R_h + R_2^c[R_h + 2R_2^w(t_f/t_c + t_f/w)]\}}$$

$$R_c^* = \frac{R_1[R_2^w R_h + R_1(R_h + 2R_2^c t_f/t_c + 2R_2^w t_f/w)]}{R_2^c R_2^w R_h + R_1{}^2(R_h + 2R_2^c t_f/t_c + 2R_2^w t_f/w) + R_1\{R_2^w R_h + R_2^c[R_h + 2R_2^w(t_f/t_c + t_f/w)]\}}$$

$$R_h^* = \frac{R_1{}^2(R_2^c - R_2^w)}{R_2^c R_2^w R_h + R_1{}^2(R_h + 2R_2^c t_f/t_c + 2R_2^w t_f/w) + R_1\{R_2^w R_h + R_2^c[R_h + 2R_2^w(t_f/t_c + t_f/w)]\}} \tag{A6}$$

Additionally, at the channel inlet,

$$\frac{T_{\mathrm{aw}} - T_{tf}^w}{T_{\mathrm{aw}} - T_f} = R_w^*$$

$$\frac{T_{\mathrm{aw}} - T_{tf}^c}{T_{\mathrm{aw}} - T_f} = R_c^* \tag{A7}$$

The coolant temperature is obtained via an energy balance

$$\rho_f c_{p,f}\dot{V}^{\mathrm{eff}}\frac{dT_f}{dz} = \frac{wq_w(z) + t_c q_c(z)}{w + t_c} \tag{A8}$$

where $\rho_f c_{p,f}$ is its volumetric specific heat. Combining with Eq. (A5) gives

$$\frac{d(T_{\mathrm{aw}} - T_f)}{dz} + \frac{1}{R_1\rho_f c_{p,f}\dot{V}^{\mathrm{eff}}}\left(\frac{w}{w+t_c}R_w^* + \frac{t_c}{w+t_c}R_c^*\right)(T_{\mathrm{aw}} - T_f) = 0 \tag{A9}$$

The solution to this differential equation yields the longitudinal distribution of the coolant temperature:

$$\frac{T_{\mathrm{aw}} - T_f}{T_{\mathrm{aw}} - T_f^0} = \exp(-\beta z) \tag{A10}$$

where

$$\beta = \frac{1}{R_1 \rho_f c_{p,f} \dot{V}^{\text{eff}}} \left(\frac{w}{w+t_c} R_w^* + \frac{t_c}{w+t_c} R_c^* \right) \tag{A11}$$

The temperature distribution on the hot face can be expressed in similar form, via Eqs. (A7) and (A10):

$$\frac{T_{\text{aw}} - T_{tf}^w}{T_{\text{aw}} - T_f^0} = R_w^* \exp(-\beta z)$$

$$\frac{T_{\text{aw}} - T_{tf}^c}{T_{\text{aw}} - T_f^0} = R_c^* \exp(-\beta z) \tag{A12}$$

All temperatures achieve their maximum at the outlet ($z=Z$).

From the preceding analysis, the temperatures at the 18 points in Fig. 5 are as follows:

$$T^{(i)} = T_{\text{aw}} - (T_{\text{aw}} - T_f^0) \cdot \begin{cases} \left(1 - \frac{1}{2}\frac{R_f}{R_1}\right) R_c^* \exp(-\beta z) & \text{at Points 1 and 10} \\ \left[R_c^* + \left(\frac{1}{2}R_c^* - R_h^* \frac{t_f}{t_c}\right)\frac{R_f}{R_1}\right] \exp(-\beta z) & \text{at Points 2 and 11} \\ \left[1 - \frac{\theta(L)}{\theta_0}\frac{R_{\text{fin}}}{R_1}\left(R_c^* - 2R_h^* \frac{t_f}{t_c}\right)\right] \exp(-\beta z) & \text{at Points 3, 4, 7, 8, 12, 13, 16, and 17} \\ \left(1 - \frac{1}{2}\frac{R_f}{R_1}\right) R_w^* \exp(-\beta z) & \text{at Points 5 and 14} \\ \left[R_w^* + \left(\frac{1}{2}R_w^* + R_h^* \frac{t_f}{w}\right)\frac{R_f}{R_1}\right] \exp(-\beta z) & \text{at Points 6 and 15} \\ \left[1 - \frac{\theta(L/2)}{\theta_0}\frac{R_{\text{fin}}}{R_1}\left(R_c^* - 2R_h^* \frac{t_f}{t_c}\right)\right] \exp(-\beta z) & \text{at Points 9 and 18} \end{cases} \tag{A13}$$

where $\theta(y)/\theta_0$ is the nondimensional fin temperature:

$$\frac{\theta(y)}{\theta_0} = \frac{T(y) - T_f}{T(0) - T_f} = \frac{\cosh\left[\sqrt{\frac{2h_C}{k_s^{\parallel} t_c}}(L-y)\right]}{\cosh\left[\sqrt{\frac{2h_C}{k_s^{\parallel} t_c}} L\right]} \tag{A14}$$

with y the coordinate oriented along the fin.

Once all the temperatures in the system are known, simple algebraic manipulation provides the temperature difference across the top face (directly above and midway between the core members):

$$\frac{\Delta T_{tf}^c(z)}{T_{\text{aw}} - T_f^0} = \left(R_c^* - R_h^* \frac{t_f}{t_c}\right)\frac{R_f}{R_1} \exp(-\beta z)$$

$$\frac{\Delta T_{tf}^w(z)}{T_{\text{aw}} - T_f^0} = \left(R_w^* + R_h^* \frac{t_f}{w}\right)\frac{R_f}{R_1} \exp(-\beta z) \tag{A15}$$

and across the entire panel (above and between the core members):

$$\frac{\Delta T_{\text{panel}}^c}{T_{\text{aw}} - T_f^0} = \left[\frac{R_2{}^c}{R_1} - \frac{R_{\text{fin}}}{R_1}\frac{\theta(L)}{\theta_0}\right]\left(R_c^* - 2R_h^* \frac{t_f}{t_c}\right) \exp(-\beta z)$$

$$\frac{\Delta T_{\text{panel}}^w}{T_{\text{aw}} - T_f^0} = \left[\left(R_w^* + 2R_h^* \frac{t_f}{w}\right)\frac{R_2{}^w}{R_1} - \left(R_c^* - 2R_h^* \frac{t_f}{t_c}\right)\frac{R_{\text{fin}}}{R_1}\frac{\theta(L)}{\theta_0}\right] \exp(-\beta z) \tag{A16}$$

Appendix B: Stress Analysis

Coolant Pressure

The coolant pressure p_f (assumed uniform along z and equal to p_f^0, given that $\Delta p \ll p_f^0$) induces uniform tensile stresses in the core members (at Points 9 and 18), given by

$$\frac{\sigma_{\text{core},y}^{p_f}}{p_f} = \frac{w}{t_c}, \quad \frac{\sigma_{\text{core},z}^{p_f}}{p_f} = \nu \frac{\sigma_{\text{core},y}^{p_f}}{p_f} \tag{B1}$$

with ν the Poisson ratio of the material. It also induces combined tension/bending in the face segments. For Boundary Condition I, these are

$$\frac{\sigma_{\text{face},x}^{p_f}}{p_f} = \begin{cases} L/2t_f + (w/t_f)^2/2 & \text{at Points 2, 3, 11, and 12} \\ L/2t_f - (w/t_f)^2/2 & \text{at Points 1, 4, 10, and 13} \\ L/2t_f + (w/t_f)^2/4 & \text{at Points 5, 8, 14, and 17} \\ L/2t_f - (w/t_f)^2/4 & \text{at Points 6, 7, 15, and 16} \end{cases}$$

$$\frac{\sigma_{\text{face},z}^{p_f}}{p_f} = \nu \frac{\sigma_{\text{face},x}^{p_f}}{p_f} \tag{B2}$$

The same solutions apply to boundary condition Type II with the exception of those for the bottom face segments, which lack the bending component. Along this face (at Points 3, 4, 7, 8, 12, 13, 16, and 17), the stresses are simply

$$\frac{\sigma_{\text{face},x}^{p_f}}{p_f} = \frac{L}{2t_f}, \quad \frac{\sigma_{\text{face},z}^{p_f}}{p_f} = \nu \frac{\sigma_{\text{face},x}^{p_f}}{p_f} \tag{B3}$$

Combustor Gas Pressure

For Boundary Condition I, the panel behaves globally as a clamped-clamped plate under uniform pressure, p_{comb}. With the usual assumption that the shear force is supported by the core and the moment by the face sheets [19], the stresses in the faces are

$$\frac{\sigma_{x,\text{face}}^{p_{\text{comb}}}}{p_{\text{comb}}} = \begin{cases} \frac{1}{12}\frac{b^2}{(H-t_f)t_f} & \text{at Points 1, 2, 5, and 6} \\ -\frac{1}{12}\frac{b^2}{(H-t_f)t_f} & \text{at Points 3, 4, 7, and 8} \\ \frac{1}{24}\frac{b^2}{(H-t_f)t_f} & \text{at Points 12, 13, 16, and 17} \\ -\frac{1}{24}\frac{b^2}{(H-t_f)t_f} & \text{at Points 10, 11, 14, and 15} \end{cases}$$

$$\frac{\sigma_{z,\text{face}}^{p_{\text{comb}}}}{p_{\text{comb}}} = \nu\frac{\sigma_{x,\text{face}}^{p_{\text{comb}}}}{p_{\text{comb}}} \tag{B4}$$

In contrast, for boundary condition Type II, bending is prohibited and, since $p_{\text{comb}} \ll p_f$, the additional stress on the top face can be neglected. For similar reasons, the stresses exerted on the core members can also be neglected for both boundary conditions.

Thermal Load

The temperature difference across the top face causes compression along its top surface and tension along its bottom surface (at the boundary with the coolant). These stresses are

$$\sigma_{\text{face},x}^{\Delta T_{tf}} = \sigma_{\text{face},z}^{\Delta T_{tf}} = \begin{cases} -\frac{E\alpha\Delta T_{tf}}{2(1-\nu)} & \text{at Points 1, 5, 10, and 14} \\ \frac{E\alpha\Delta T_{tf}}{2(1-\nu)} & \text{at Points 2, 6, 11, and 15} \end{cases} \tag{B5}$$

with E and α the Young modulus and the coefficient of thermal expansion of the material, respectively. Additionally, the average temperature difference between the top and bottom faces, $\Delta T_{\text{panel}} = (\Delta T_{\text{panel}}^{w} + \Delta T_{\text{panel}}^{c})/2$, causes the panel to deform uniformly in each of the x- and z-directions, inducing compression in the top face and tension in the bottom face [17]. Accounting for the stretching stiffness of the core members along the z-direction and assuming that the temperatures of the core and the bottom face are the same at steady state, the resulting additional stresses are

$$\sigma_{\text{face},x}^{\Delta T_{\text{panel}}} = \begin{cases} -\frac{E\alpha\Delta T_{\text{panel}}}{2(1-\nu)} & \text{at Points 1, 2, 5, 6, 10, 11, 14, and 15} \\ \frac{E\alpha\Delta T_{\text{panel}}}{2(1-\nu)} & \text{at Points 3, 4, 7, 8, 12, 13, 16, and 17} \end{cases}$$

$$\sigma_{\text{face},z}^{\Delta T_{\text{panel}}} = \begin{cases} -\frac{E\alpha\Delta T_{\text{panel}}(A_f + A_c)}{(1-\nu)(2A_f + A_c)} & \text{at Points 1, 2, 5, 6, 10, 11, 14, and 15} \\ \frac{E\alpha\Delta T_{\text{panel}}A_f}{(1-\nu)(2A_f + A_c)} & \text{at Points 3, 4, 7, 8, 12, 13, 16, and 17} \end{cases} \tag{B6}$$

where $A_f = t_f(w + t_c)$ and $A_c = (H - 2t_f)t_c$ are the cross-sectional areas of the face and the core in a unit cell, respectively. These results apply to both boundary conditions.

Failure Conditions

For metals, failure is defined as the onset of yielding. The von Mises criterion is used, namely,

$$\max_{i=1-18}\left\{\left(\frac{\sigma_{m,x}^{(i)}}{\sigma_Y(T^{(i)})} + \frac{\sigma_{T,x}^{(i)}}{\sigma_Y(T^{(i)})} - \frac{\sigma_{m,z}^{(i)}}{\sigma_Y(T^{(i)})} - \frac{\sigma_{T,z}^{(i)}}{\sigma_Y(T^{(i)})}\right)^2 + \left(\frac{\sigma_{m,x}^{(i)}}{\sigma_Y(T^{(i)})} + \frac{\sigma_{T,x}^{(i)}}{\sigma_Y(T^{(i)})}\right)^2 + \left(\frac{\sigma_{m,z}^{(i)}}{\sigma_Y(T^{(i)})} + \frac{\sigma_{T,z}^{(i)}}{\sigma_Y(T^{(i)})}\right)^2\right\} = 2 \tag{B7}$$

with the stress components and the temperature at each location i given by Eqs. (B2)–(B6) and (A13), respectively. The yield strength of the material σ_Y is assumed to linearly decrease with temperature (Table 2).

Well-designed CMCs typically fail when the *normal stress* along the primary fiber orientation attains either the ultimate tensile strength or the compressive strength. Assuming for simplicity that the strengths in tension and compression are identical and temperature independent (reasonable for SiC/SiC and C/SiC [34,35]), the ensuing condition is

$$\max_{i=1-18}\left\{\max\left\{\frac{|\sigma_{m,x}^{(i)} + \sigma_{T,x}^{(i)}|}{\sigma_{\text{ult}}}, \frac{|\sigma_{m,z}^{(i)} + \sigma_{T,z}^{(i)}|}{\sigma_{\text{ult}}}\right\}\right\} = 1 \tag{B8}$$

Pressure Drop

The pressure drop in the coolant due to viscous dissipation over the length of the panel is [32]

$$\Delta p = \frac{2\rho_f f Z(\dot{V}^{\text{eff}})^2}{H^2(1-\bar{\rho})^2 D_h} \tag{B9}$$

with $\bar{\rho} = 1 - Lw/[H(w + t_c)]$ the relative density of the panel.

References

[1] Steeves, C. A., He, M. Y., Valdevit, L., Kasen, S. D., Wadley, H. N. G., and Evans, A. G., 2008, "Feasibility of Metallic Structural Heat Pipes as Sharp Leading Edges for Hypersonic Vehicles," ASME J. Appl. Mech., in press.

[2] Curran, E. T., and Murthy, S. N. B., 2000, *Scramjet Propulsion*, American Institute of Aeronautics and Astronautics, Reston, VA.

[3] Heiser, W. H., and Pratt, D. T., 1994, *Hypersonic Airbreathing Propulsion*, AIAA, Washington, DC.

[4] Bertin, J. J., 1994, *Hypersonic Aerothermodynamics*, American Institute of Aeronautics and Astronautics, Washington, DC.

[5] Buchmann, O. A., 1979, "Thermal-Structural Design Study of an Airframe-Integrated Scramjet," Technical Report No. NASA 3141.

[6] Rakow, J. F., and Waas, A. M., 2005, "Thermal Buckling of Metal Foam Sandwich Panels for Convective Thermal Protection Systems," J. Spacecr. Rockets, **42**(5), pp. 832–844.

[7] Rakow, J. F., and Waas, A. M., 2005, "Thermomechanical Response of Actively Cooled Metal Foam Sandwich Panels for Thermal Protection Systems," 46th AIAA/ASME/ASCE/AHS/ASC Structures, Structural Dynamics & Materials Conference, AIAA, Austin, TX.

[8] Song, K. D., Choi, S. H., and Scotti, S. J., 2006, "Transpiration Cooling Experiment for Scramjet Engine Combustion Chamber by High Heat Fluxes," J. Propul. Power, **22**(1), pp. 96–102.

[9] Scotti, S. J., Martin, C. J., and Lucas, S. H., 1988, "Active Cooling Design for

Scramjet Engines Using Optimization Methods," Technical Report No. NASA 100581.
[10] Youn, B., and Mills, A. F., 1995, "Cooling Panel Optimization for the Active Cooling System of a Hypersonic Aircraft," J. Thermophys. Heat Transfer, **9**(1), pp. 136–143.
[11] Flieder, W. C., Richard, C. E., Buchmann, O. A., and Walters, F. M., 1971, "An Analytical Study of Hydrogen Cooled Panels for Application to Hypersonic Aircraft," Technical Report No. NASA CR-1650.
[12] Walters, F. M., and Buchmann, O. A., 1971, "Heat Transfer and Fluid Flow Analysis of Hydrogen-Cooled Panels and Manifold Systems," Technical Report No. NASA CR-66925.
[13] Evans, A. G., Mumm, D. R., Hutchinson, J. W., Meier, G. H., and Pettit, F. S., 2001, "Mechanisms Controlling the Durability of Thermal Barrier Coatings," Prog. Mater. Sci., **46**(5), pp. 505–553.
[14] Gnielinski, V., 1976, "New Equations for Heat and Mass-Transfer in Turbulent Pipe and Channel Flow," Int. Chem. Eng., **16**(2), pp. 359–368.
[15] Bree, J., 1969, "Incremental Growth Due to Creep and Plastic Yielding of Thin Tubes Subjected to Internal Pressure and Cyclic Thermal Stresses," J. Strain Anal., **3**(2), pp. 122–127.
[16] Bree, J., 1989, "Plastic-Deformation of a Closed Tube Due to Interaction of Pressure Stresses and Cyclic Thermal-Stresses," Int. J. Mech. Sci., **31**(11–12), pp. 865–892.
[17] Boley, B. A., and Weiner, J. H., 1960, *Theory of Thermal Stresses*, Wiley, New York.
[18] Rathbun, H. J., Zok, F. W., and Evans, A. G., 2005, "Strength Optimization of Metallic Sandwich Panels Subject to Bending," Int. J. Solids Struct., **42**(26), pp. 6643–6661.
[19] Valdevit, L., Hutchinson, J. W., and Evans, A. G., 2004, "Structurally Optimized Sandwich Panels With Prismatic Cores," Int. J. Solids Struct., **41**(18–19), pp. 5105–5124.
[20] Valdevit, L., Wei, Z., Mercer, C., Zok, F. W., and Evans, A. G., 2006, "Structural Performance of Near-Optimal Sandwich Panels With Corrugated Cores," Int. J. Solids Struct., **43**(16), pp. 4888–4905.
[21] Wei, Z., Zok, F. W., and Evans, A. G., 2006, "Design of Sandwich Panels With Prismatic Cores," ASME J. Eng. Mater. Technol., **128**(2), pp. 186–192.
[22] Wicks, N., and Hutchinson, J. W., 2001, "Optimal Truss Plates," Int. J. Solids Struct., **38**(30–31), pp. 5165–5183.
[23] Wicks, N., and Hutchinson, J. W., 2004, "Performance of Sandwich Plates With Truss Cores," Mech. Mater., **36**(8), pp. 739–751.
[24] Zok, F. W., Rathbun, H., He, M., Ferri, E., Mercer, C., McMeeking, R. M., and Evans, A. G., 2005, "Structural Performance of Metallic Sandwich Panels With Square Honeycomb Cores," Philos. Mag., **85**(26–27), pp. 3207–3234.
[25] Zok, F. W., Rathbun, H. J., Wei, Z., and Evans, A. G., 2003, "Design of Metallic Textile Core Sandwich Panels," Int. J. Solids Struct., **40**(21), pp. 5707–5722.
[26] Zok, F. W., Waltner, S. A., Wei, Z., Rathbun, H. J., McMeeking, R. M., and Evans, A. G., 2004, "A Protocol for Characterizing the Structural Performance of Metallic Sandwich Panels: Application to Pyramidal Truss Cores," Int. J. Solids Struct., **41**(22–23), pp. 6249–6271.
[27] National Research Council (US) Committee on the National Aerospace Initiative, 2004, *Evaluation of the National Aerospace Initiative*, National Academy, Washington, DC.
[28] Novak, M. D., and Levi, C. G., 2007, "Oxidation and Volatilization of Silicide Coatings for Refractory Niobium Alloys," ASME IMECE, Seattle, WA.
[29] Marshall, D. B., personal communication.
[30] Lu, T. J., Valdevit, L., and Evans, A. G., 2005, "Active Cooling by Metallic Sandwich Structures With Periodic Cores," Prog. Mater. Sci., **50**(7), pp. 789–815.
[31] Valdevit, L., Pantano, A., Stone, H. A., and Evans, A. G., 2006, "Optimal Active Cooling Performance of Metallic Sandwich Panels With Prismatic Cores," Int. J. Heat Mass Transfer, **49**(21–22), pp. 3819–3830.
[32] Bejan, A., 2004, *Convection Heat Transfer*, Wiley, Hoboken, NJ.
[33] Moody, L. F., 1944, "Friction Factors for Pipe Flow," Trans. ASME, **66**, pp. 671–684.
[34] Wang, M., and Laird, C., 1996, "Characterization of Microstructure and Tensile Behavior of a Cross-Woven C–SiC Composite," Acta Mater., **44**(4), pp. 1371–1387.
[35] Wang, M. D., and Laird, C., 1996, "Damage and Fracture of a Cross Woven C/SiC Composite Subject to Compression Loading," J. Mater. Sci., **31**(8), pp. 2065–2069.